

FEM Spatial Extension of the Hamilton Biofilm Model

From 0-D TMCMC Parameter Estimation to 1-D / 2-D / 3-D Reaction-Diffusion Simulation

Nishioka
IKM Hiwi

2026-02-21

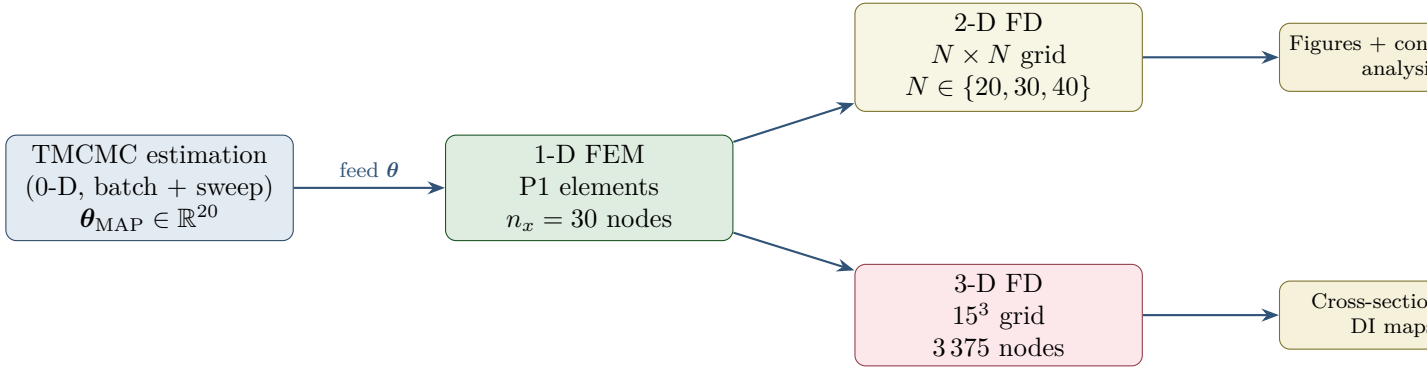
Contents

1	Overview	2
1.1	Biological Conditions	2
2	Mathematical Background	2
2.1	Hamilton 0-D Biofilm Model	2
2.2	Reaction-Diffusion PDE	3
2.3	Operator Splitting (Lie)	3
2.4	Spatial Discretisation	3
3	Implementation	4
3.1	File Structure	4
3.2	Numba Parallel Reaction Kernel	4
3.3	Initial Conditions (<code>-init-mode gradient</code>)	4
4	One-Dimensional Results	5
4.1	<code>dh_baseline</code> — Dysbiotic Condition	5
4.2	Commensal Static — Balanced Condition	7
4.3	1-D Condition Comparison	9
5	Two-Dimensional Results	10
5.1	<code>dh_baseline</code>	10
5.2	Commensal Static	13
5.3	Side-by-Side Lateral Profile Comparison	16
6	Mesh Convergence Analysis (2-D)	16
6.1	Domain-Averaged Dynamics	16
6.2	Spatial Structure and Convergence Diagnostics	16
7	Three-Dimensional Results	18
7.1	<code>dh_baseline</code>	18
7.2	Commensal Static	21
7.3	3-D Cross-Section Comparison	24
8	Performance	24
9	Usage Summary	24
9.1	Running Simulations	24
9.2	Mesh Convergence Test	25

10 Summary and Outlook	25
10.1 Achievements	25
10.2 Potential Next Steps	26
A Laplacian Matrix Construction	26
B Parameter Index Map	27
C Dysbiotic Index Definition	27

1 Overview

The goal of this work is to embed the five-species Hamilton biofilm ODE — whose 20 parameters are inferred by TMCMC in `Tmcmc202601/data_5species/` — inside a spatial reaction-diffusion framework and to compare the resulting spatio-temporal patterns for two biologically distinct conditions.



1.1 Biological Conditions

Two θ_{MAP} vectors from different TMCMC runs are used:

Parameter	dh_baseline	Commensal Static	Biological role
a_{23}	21.0	2.69	A. naeslundii → Veillonella cross-feeding
a_{35}	21.4	1.37	Veillonella → P. gingivalis support
a_{45}	2.50	2.79	F. nucleatum → P. gingivalis support
a_{55}	0.12	2.62	P. gingivalis self-growth
Character	extreme ($a_{23}, a_{35} \gg 1$)	balanced (≤ 2.79)	

Dysbiotic alert. In **dh_baseline** the large a_{23} and a_{35} create a commensal cascade (A.n → Vei → P.g) that drives strong P.gingivalis growth even when a_{55} is small. This is the dysbiotic scenario.

2 Mathematical Background

2.1 Hamilton 0-D Biofilm Model

The state vector is $\mathbf{g} = (\phi_1, \dots, \phi_5, \phi_0, \psi_1, \dots, \psi_5, \gamma)^\top \in \mathbb{R}^{12}$ where ϕ_i are volume fractions and $\phi_0 = 1 - \sum_{i=1}^5 \phi_i$ is the void (water) fraction. The 20-dimensional parameter vector $\boldsymbol{\theta}$ is partitioned as:

Block	Parameters	Species	Role
M1	$a_{11}, a_{12}, a_{22}, b_1, b_2$	<i>S. oralis</i> , <i>A. naeslundii</i>	self/mutual interaction
M2	$a_{33}, a_{34}, a_{44}, b_3, b_4$	<i>Veillonella</i> , <i>F. nucleatum</i>	self/mutual interaction
M3	$a_{13}, a_{14}, a_{23}, a_{24}$	cross-commensal	early-coloniser cross-feeding
M4	a_{55}, b_5	<i>P. gingivalis</i>	pathogen self-growth
M5	$a_{15}, a_{25}, a_{35}, a_{45}$	P.g cross-support	commensal → pathogen support

At each implicit time step the residual $\mathbf{Q}(\mathbf{g}^{n+1}; \mathbf{g}^n, \boldsymbol{\theta}) = \mathbf{0}$ is solved by Newton iteration with line-search backtracking (`_newton_step_jit`, Numba JIT).

2.2 Reaction-Diffusion PDE

Each species volume fraction satisfies:

$$\frac{\partial \phi_i}{\partial t} = \underbrace{R_i(\phi, \psi, \gamma; \theta)}_{\text{Hamilton reaction}} + D_i \nabla^2 \phi_i, \quad i = 1, \dots, 5, \quad (1)$$

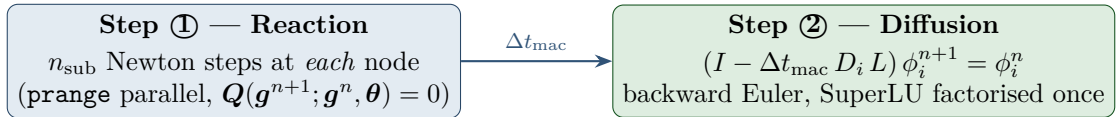
with no-flux (Neumann) BCs on all walls. Default diffusion coefficients (motility proxies):

Species	D_i	Notes
<i>S. oralis</i> , <i>A. naeslundii</i>	1×10^{-3}	fast commensal spreading
<i>Veillonella</i>	8×10^{-4}	
<i>F. nucleatum</i>	5×10^{-4}	bridge species
<i>P. gingivalis</i>	2×10^{-4}	slowest (pathogen)

The Hamilton time variable t used here is non-dimensional: the macro step size is $\Delta t_{\text{mac}} = n_{\text{sub}} \Delta t_h$ and the total horizon $t_{\text{tot}} = n_{\text{macro}} \Delta t_{\text{mac}} = 0.05$ corresponds to the late-time window of the underlying TMCMC-calibrated ODE model. Connecting t to physical hours or days requires an additional calibration step against experimental growth curves and is left as future work; throughout this report we interpret t qualitatively as *early* vs. *late* biofilm stages.

2.3 Operator Splitting (Lie)

Each macro time step $\Delta t_{\text{mac}} = \Delta t_h \times n_{\text{sub}}$ is split as:



This Lie splitting is first-order accurate in time ($\mathcal{O}(\Delta t_{\text{mac}})$). After each diffusion step the volume constraint is enforced: $\phi_0 \leftarrow \max(0, 1 - \sum_i \phi_i)$.

2.4 Spatial Discretisation

1-D (P1 finite elements, uniform mesh).

$$(M + \Delta t_{\text{mac}} D_i K) \phi^{n+1} = M \phi^n,$$

where M is the consistent mass matrix and K the stiffness matrix.

2-D and 3-D (finite differences, uniform grid). The 1-D Neumann Laplacian with ghost-node half-stencil at the walls is

$$[L]_{jj} = \begin{cases} -1/h^2 & j = 0 \text{ or } N-1, \\ -2/h^2 & \text{otherwise,} \end{cases} \quad [L]_{j,j\pm 1} = 1/h^2. \quad (2)$$

Node ordering $k = i_x N_y + i_y$ (2-D) or $k = i_x N_y N_z + i_y N_z + i_z$ (3-D) gives:

$$L_{\text{2D}} = L_x \otimes I_y + I_x \otimes L_y, \quad (3)$$

$$L_{\text{3D}} = (L_x \otimes I_y) \otimes I_z + (I_x \otimes L_y) \otimes I_z + (I_x \otimes I_y) \otimes L_z. \quad (4)$$

The backward-Euler system $(I - \Delta t_{\text{mac}} D_i L) \phi^{n+1} = \phi^n$ is solved per species via SuperLU (factorised once at initialisation).

In 1-D the FEM formulation is convenient for reusing standard mass and stiffness matrices and for potential extension to non-uniform meshes. In 2-D and 3-D a finite-difference discretisation is used for simplicity and efficiency; the resulting discrete Laplacians are algebraically equivalent to the FEM Laplacian on a uniform grid with the same Neumann boundary treatment.

3 Implementation

3.1 File Structure

File	Role
fem_spatial_extension.py	1-D simulation (P1 FEM)
fem_visualize.py	1-D visualisation — 8 figures
fem_2d_extension.py	2-D simulation (FD)
fem_2d_visualize.py	2-D visualisation — 5 figures
fem_3d_extension.py	3-D simulation (FD)
fem_3d_visualize.py	3-D visualisation — 5 figures
fem_convergence.py	mesh convergence analysis + Markdown report
FEM_README.md	full inline documentation
fem_report.tex / .pdf	this document

3.2 Numba Parallel Reaction Kernel

```

1 @njit(parallel=True, cache=False)
2 def _reaction_step(G_flat, A, b_diag, n_sub, dt_h,
3                     Kp1, Eta_vec, Eta_phi_vec, c_val, alpha_val,
4                     K_hill, n_hill, eps_tol, active_mask):
5     N = G_flat.shape[0]                      # Nx*Ny or Nx*Ny*Nz
6     G_out = np.empty_like(G_flat)
7     for k in prange(N):                      # parallel over all nodes
8         g = G_flat[k].copy()
9         g_new_buf = np.zeros(12)   # per-thread buffers (no race condition)
10        K_buf      = np.zeros((12, 12))
11        Q_buf      = np.zeros(12)
12        for _ in range(n_sub):    # Hamilton sub-steps
13            _newton_step_jit(g, dt_h, Kp1, Eta_vec, Eta_phi_vec,
14                                c_val, alpha_val, K_hill, n_hill,
15                                A, b_diag, eps_tol, 50,
16                                active_mask, g_new_buf, K_buf, Q_buf)
17        g[:] = g_new_buf[:]
18        G_out[k] = g
19    return G_out

```

Listing 1: Parallel reaction kernel (identical for 2-D and 3-D). Each worker thread has its own Newton buffers to avoid race conditions.

3.3 Initial Conditions (-init-mode gradient)

Species	Initial profile
<i>S.oralis</i> , <i>A.naeslundii</i> , <i>Veillonella</i>	$\phi_i^0 = 0.10 + \varepsilon$, uniform with small noise
<i>F.nucleatum</i>	$0.05 e^{-3x/L_x} + \varepsilon$ (surface-enriched)
<i>P.gingivalis</i> (1-D)	$0.01 e^{-5x/L_x} + \varepsilon$
<i>P.gingivalis</i> (2-D)	$0.01 e^{-5x/L_x} \cdot G_\sigma(y - y_c)$
<i>P.gingivalis</i> (3-D)	$0.01 e^{-5x/L_x} \cdot G_\sigma(y - y_c) \cdot G_\sigma(z - z_c)$

G_σ is a Gaussian with $\sigma = 0.1 L$; $x = 0$ is the substratum surface. In the 2-D and 3-D implementations, ε is realised as small zero-mean Gaussian perturbations with standard deviations 10^{-2} for the commensal species, 5×10^{-3} for *Veillonella* and *F.nucleatum*, and 2×10^{-3} for *P.gingivalis* (clipped to keep $\phi_i \geq 0$). The void fraction ϕ_0 is then set to $1 - \sum_i \phi_i$ so that the total volume fraction remains bounded by 1 everywhere.

4 One-Dimensional Results

4.1 dh_baseline — Dysbiotic Condition

The 1-D simulation uses 30 nodes on a depth domain $[0, L_x]$, 100 macro steps ($\Delta t_{\text{mac}} = 5 \times 10^{-4}$), and 50 Hamilton sub-steps.

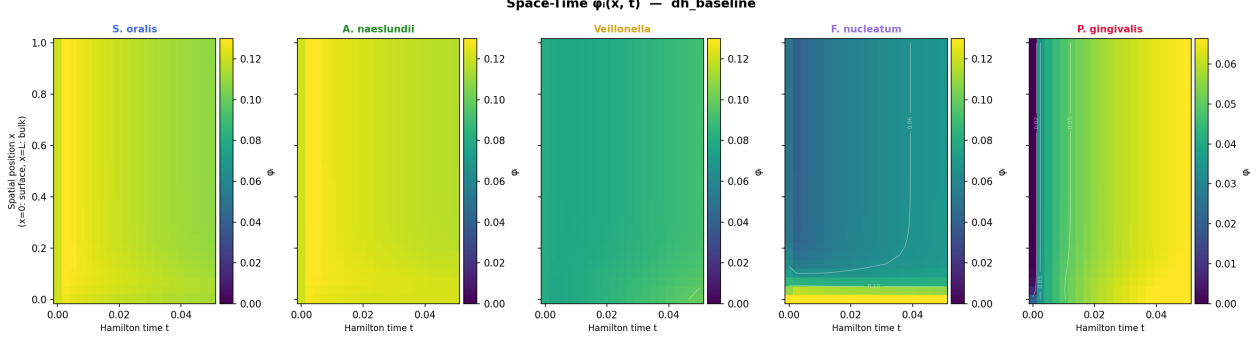
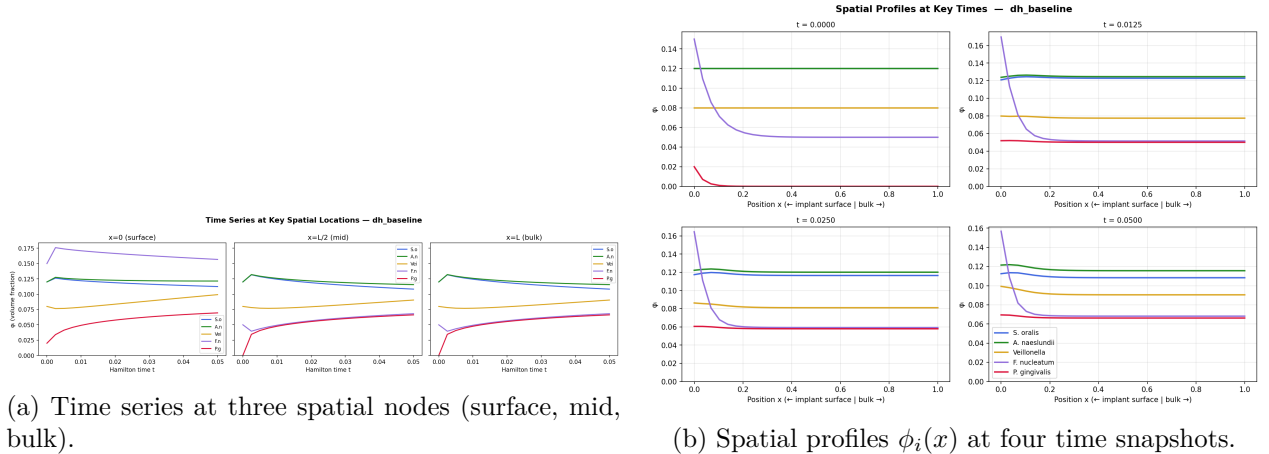


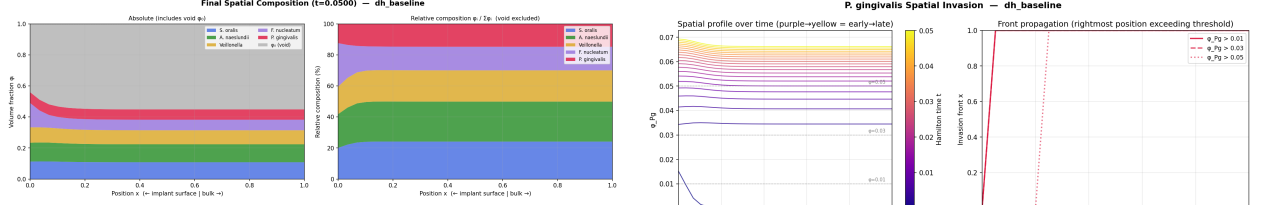
Figure 1: **1-D space-time heatmaps — dh_baseline.** Each panel shows $\phi_i(x, t)$ as a colour map (depth x on vertical axis, time t on horizontal axis). *S.oralis* and *A.naeslundii* decline at the surface as *P.gingivalis* accumulates near $x = 0$, driven by the large cascade parameters $a_{23} = 21$, $a_{35} = 21$.



(a) Time series at three spatial nodes (surface, mid, bulk).

(b) Spatial profiles $\phi_i(x)$ at four time snapshots.

Figure 2: **dh_baseline — temporal and spatial dynamics.** Left: the surface node (closest to substratum) shows the fastest P.g rise. Right: the gradient sharpens over time as P.g migrates toward $x = 0$.



(a) Final composition: stacked area (absolute + relative %).

(b) P.g invasion front $x_{\text{front}}(t)$ (iso-contour tracking).

Figure 3: **dh_baseline — final composition and pathogen front.** P.gingivalis occupies $\sim 10\%$ of the total volume at t_{final} and is strongly surface-enriched. The invasion front advances monotonically from the surface into the bulk.

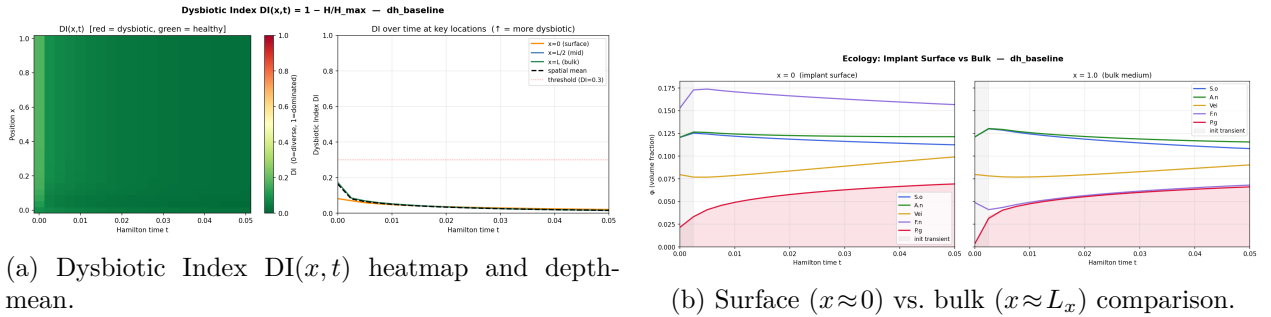


Figure 4: **dh_baseline — dysbiosis quantification.** $DI = 1 - H/H_{\text{max}}$ where $H = -\sum p_i \ln p_i$; $DI \rightarrow 0$ (balanced), $DI \rightarrow 1$ (single-species dominance). The surface layer develops significantly higher DI than the bulk, reflecting the depth-localised P.g accumulation.

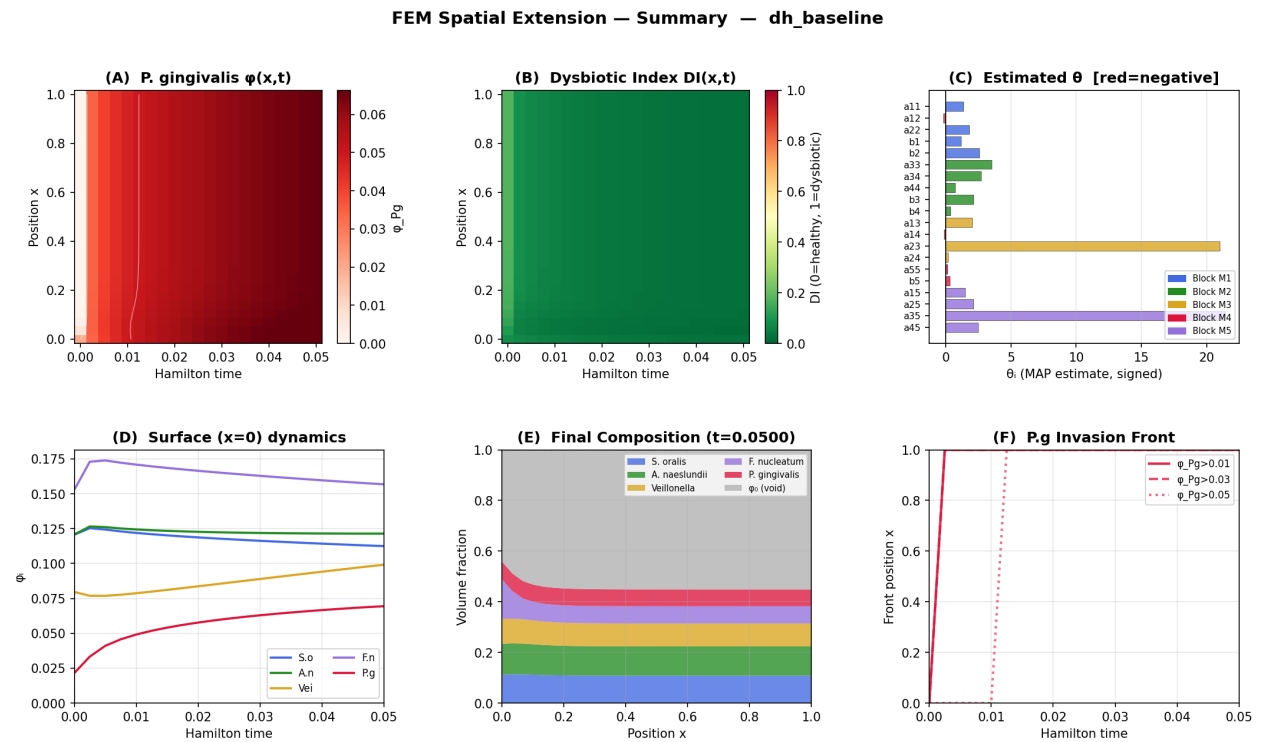


Figure 5: **1-D dh_baseline — six-panel summary.** Clockwise from top-left: space-time heatmap, spatial profile at t_{final} , parameter bar chart (θ_{MAP}), DI time series, final stacked composition, surface vs. bulk volume fractions.

4.2 Commensal Static — Balanced Condition

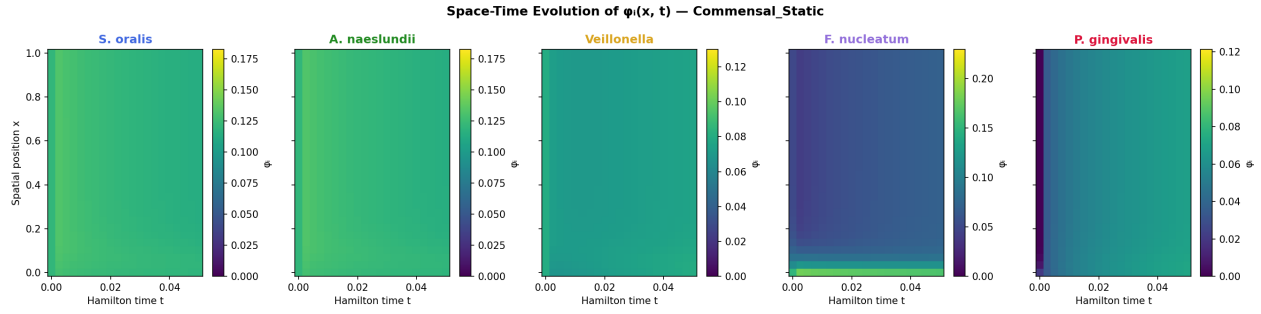


Figure 6: **1-D space-time heatmaps — Commensal Static.** All five species coexist with gentle gradients throughout the simulation. $P. gingivalis$ remains low ($\bar{\phi}_{P.g} \approx 0.07$) and does not dominate the surface layer, in stark contrast to dh_baseline.

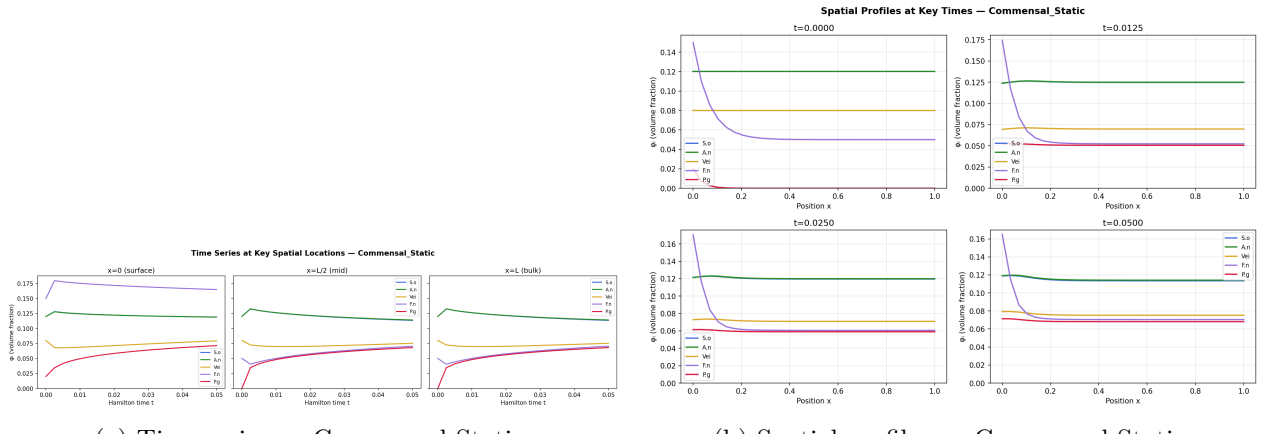
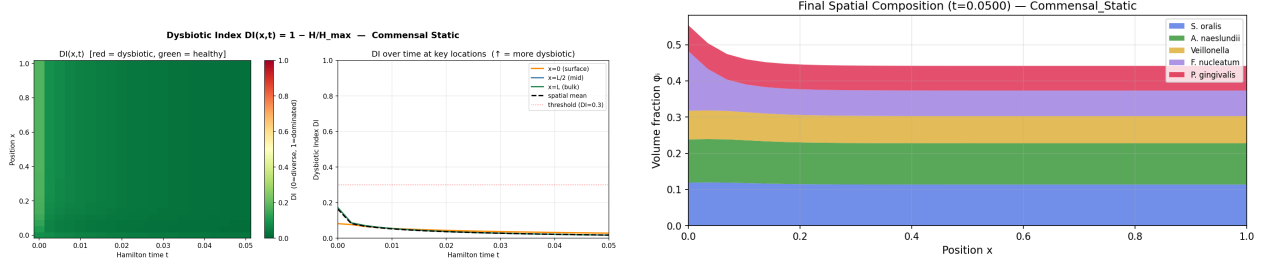


Figure 7: **Commensal Static — temporal and spatial dynamics.** Species trajectories reach a near-steady state by $t \approx 0.02$ with very shallow spatial gradients, consistent with a balanced biofilm.



(a) DI — Commensal Static: remains near zero.

(b) Final composition — Commensal Static.

Figure 8: **Commensal Static — DI and final composition.** DI stays close to 0 throughout, confirming high Shannon diversity. The five species share the biofilm volume roughly equally.

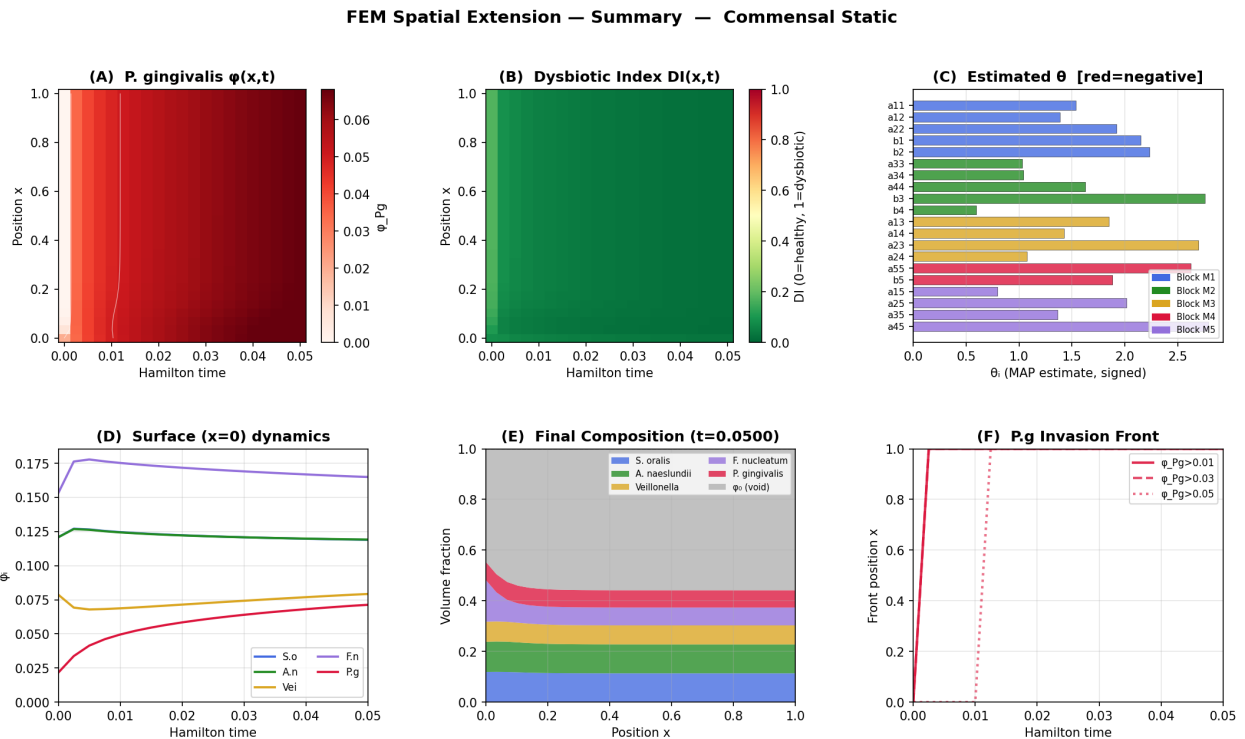
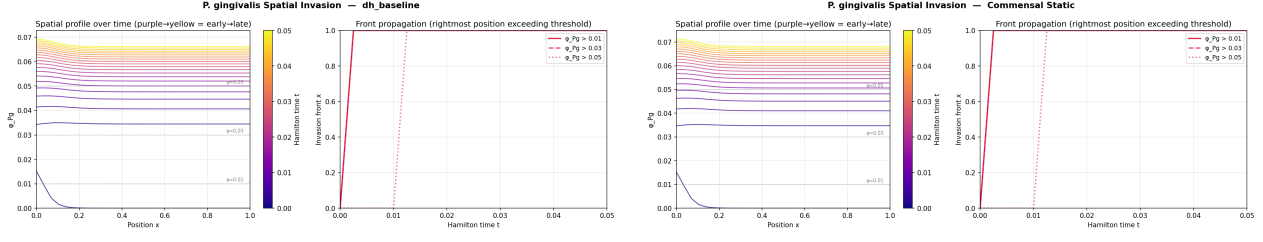


Figure 9: **1-D Commensal Static — six-panel summary.** The parameter bar chart (bottom right) shows all $\theta_i \leq 2.79$, confirming the balanced parameter regime.

4.3 1-D Condition Comparison

Key insight. The 1-D simulations confirm that the two conditions produce qualitatively different spatial dynamics: **dh_baseline** generates a pronounced surface accumulation of P.g and rising DI, while **Commensal Static** maintains near-uniform species distributions and near-zero DI throughout the domain.



(a) **dh_baseline**: monotone P.g front advance. (b) **Commensal Static**: no discernible invasion front.

Figure 10: **P.gingivalis invasion front — side-by-side comparison.** The front tracking iso-contour is meaningful only in dh_baseline, where P.g advances $\approx 35\%$ of the domain depth over $t \in [0, 0.05]$.

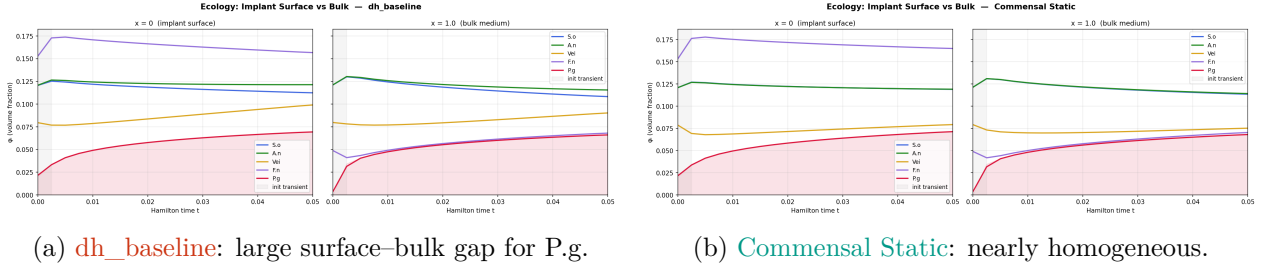


Figure 11: **Surface vs. bulk dynamics — comparison.** dh_baseline shows a growing surface–bulk divergence; Commensal Static remains spatially uniform, reflecting the absence of a focused P.g cascade.

5 Two-Dimensional Results

The 2-D simulation uses a uniform 20×20 grid on the domain $[0, L_x] \times [0, L_y]$ ($L_x = L_y = 1$). The depth axis (x) runs vertically with $x = 0$ at the substratum; the lateral axis (y) is horizontal.

5.1 dh_baseline

2D Species Distribution | dh_baseline

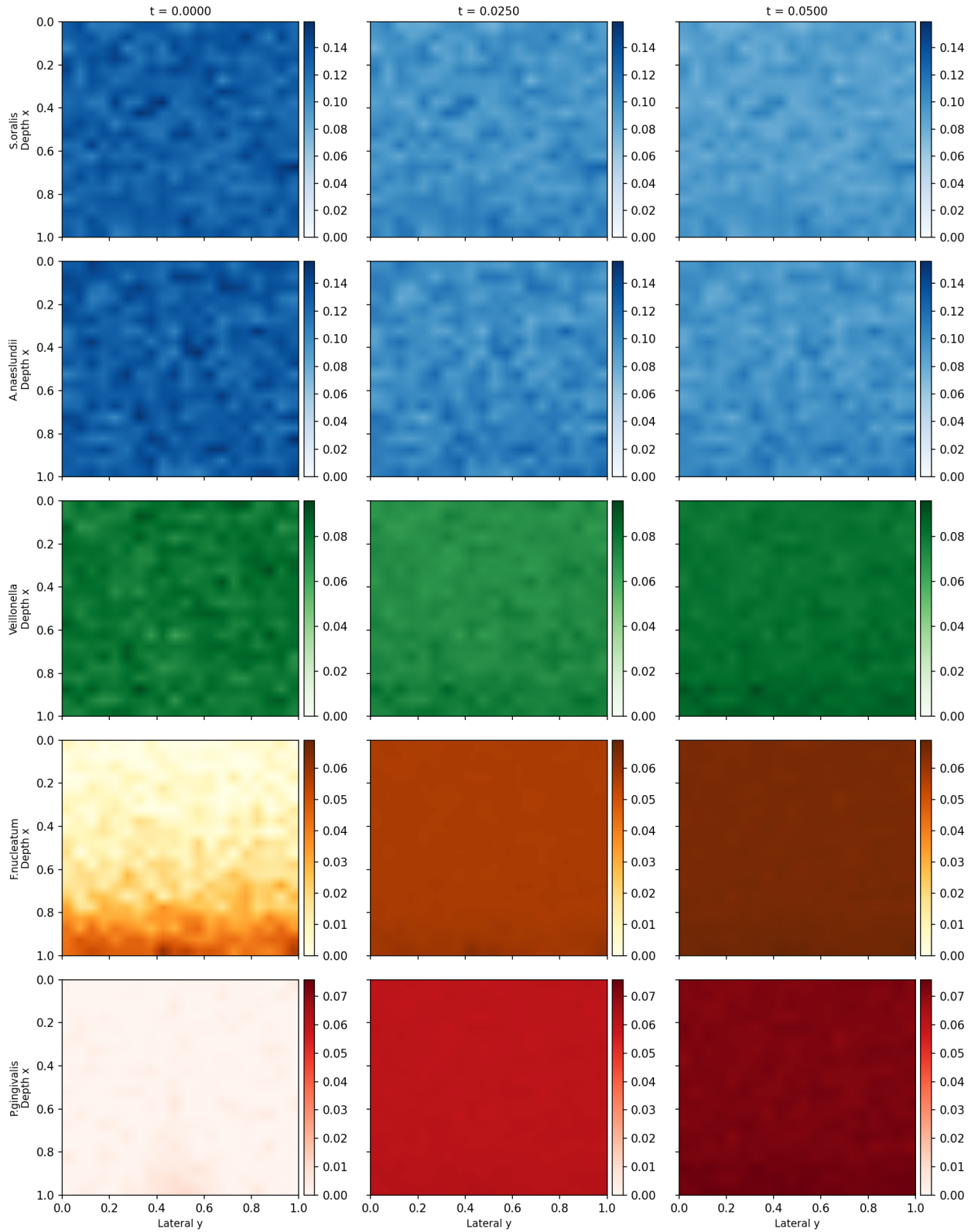


Figure 12: **2-D spatial distribution — dh_baseline.** Each row is one species; each column a time snapshot. *F.nucleatum* (row 4) shows a strong depth gradient throughout; *P.gingivalis* (row 5) grows from the focal seed at ($x \approx 0$, $y = 0.5$) and spreads both laterally and into depth.

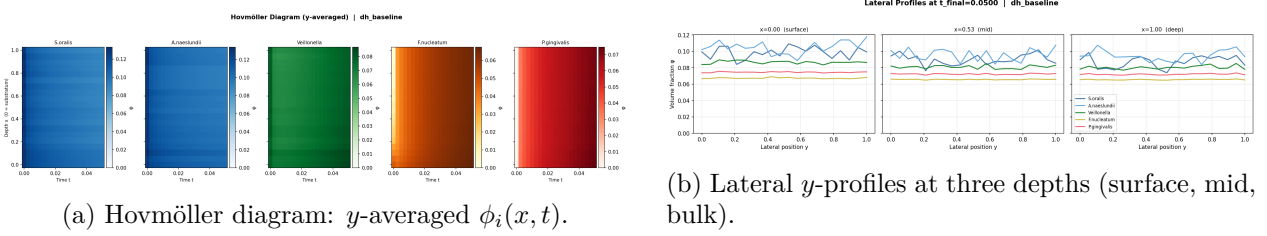


Figure 13: **dh_baseline — Hovmöller and lateral profiles.** The Hovmöller (left) confirms the depth gradient seen in 1-D; the lateral profiles (right) show that the P.g focal seed creates a lateral asymmetry that persists at the surface layer.

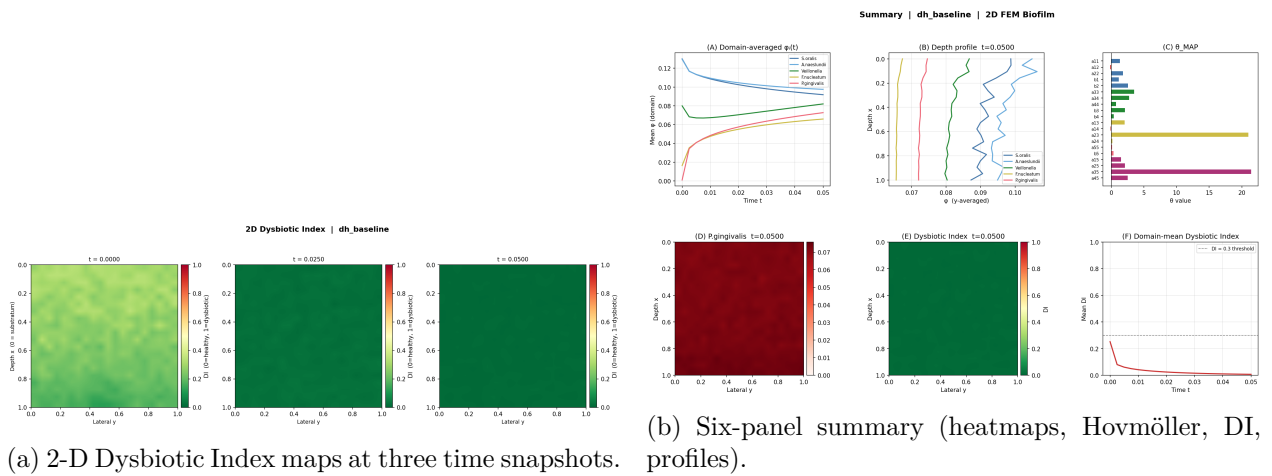


Figure 14: **dh_baseline — 2-D dysbiotic index and summary.** The DI maps reveal that dysbiosis is spatially localised near the substratum ($x = 0$) and near the lateral centre where the P.g seed was placed. By t_{final} the high-DI region has expanded significantly.

5.2 Commensal Static

2D Species Distribution | Commensal Static

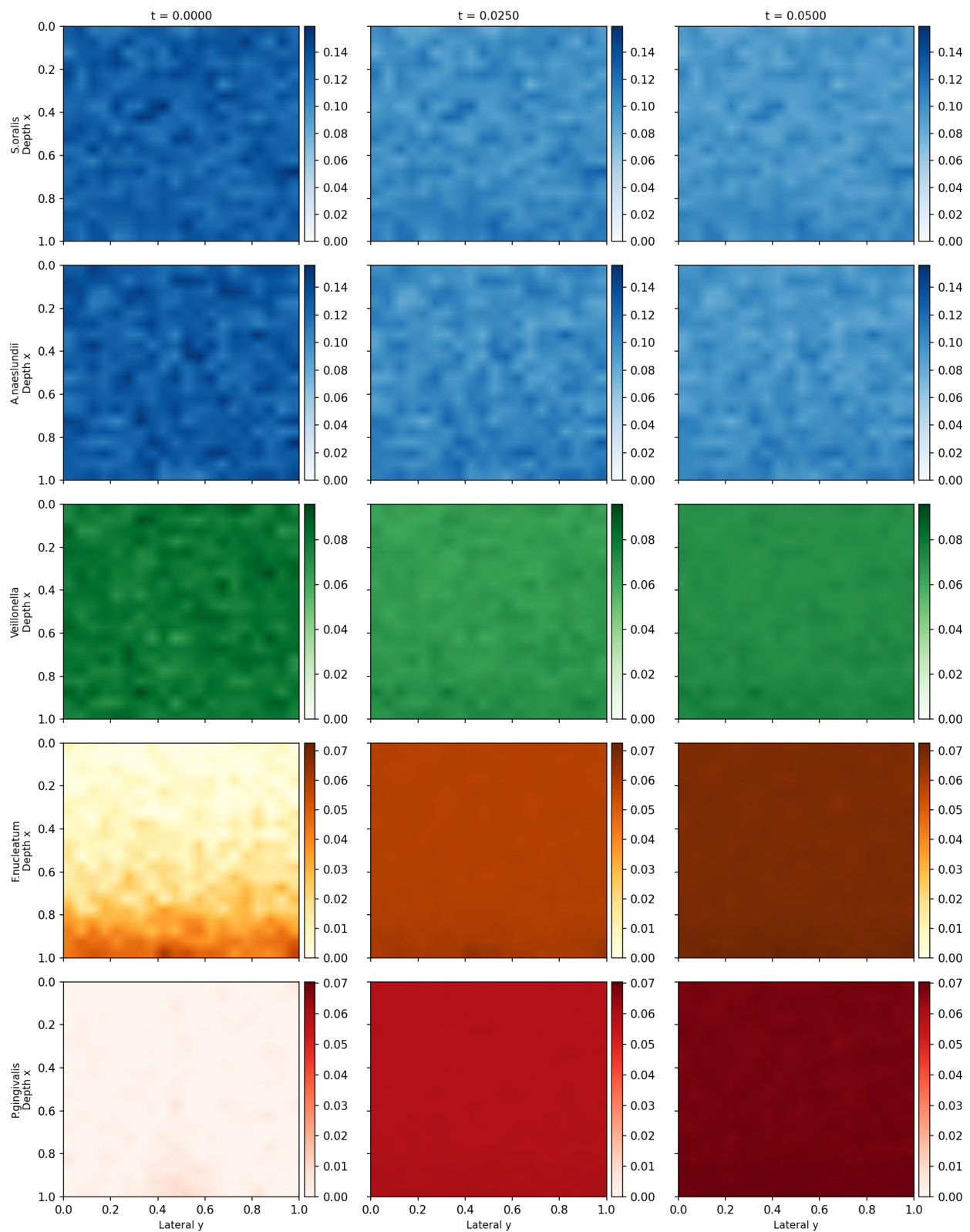
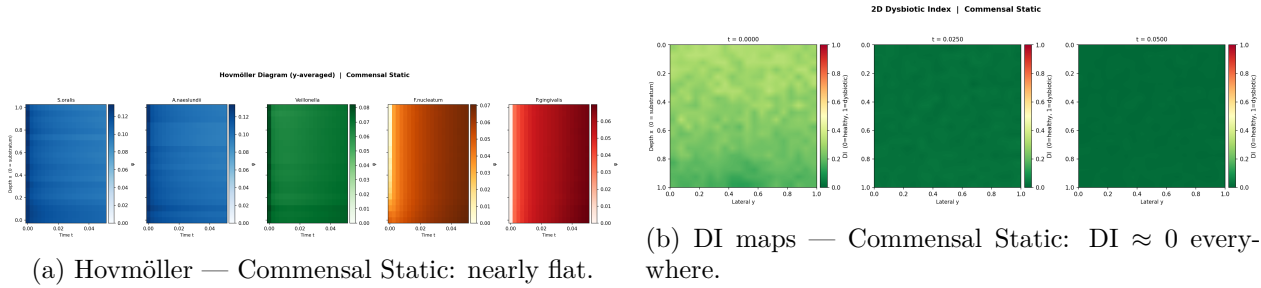


Figure 15: **2-D spatial distribution — Commensal Static.** All five species maintain gentle gradients with no pathogenic accumulation. The *F.n* depth gradient persists (same IC) but remains mild; *P.g* stays near its initial focal seed and does not spread aggressively.



(a) Hovmöller — Commensal Static: nearly flat.

(b) DI maps — Commensal Static: $\text{DI} \approx 0$ everywhere.

Figure 16: **Commensal Static — Hovmöller and 2-D DI.** Flat Hovmöller confirms spatial homogeneity. DI maps show essentially zero dysbiosis across the entire domain at all time points.

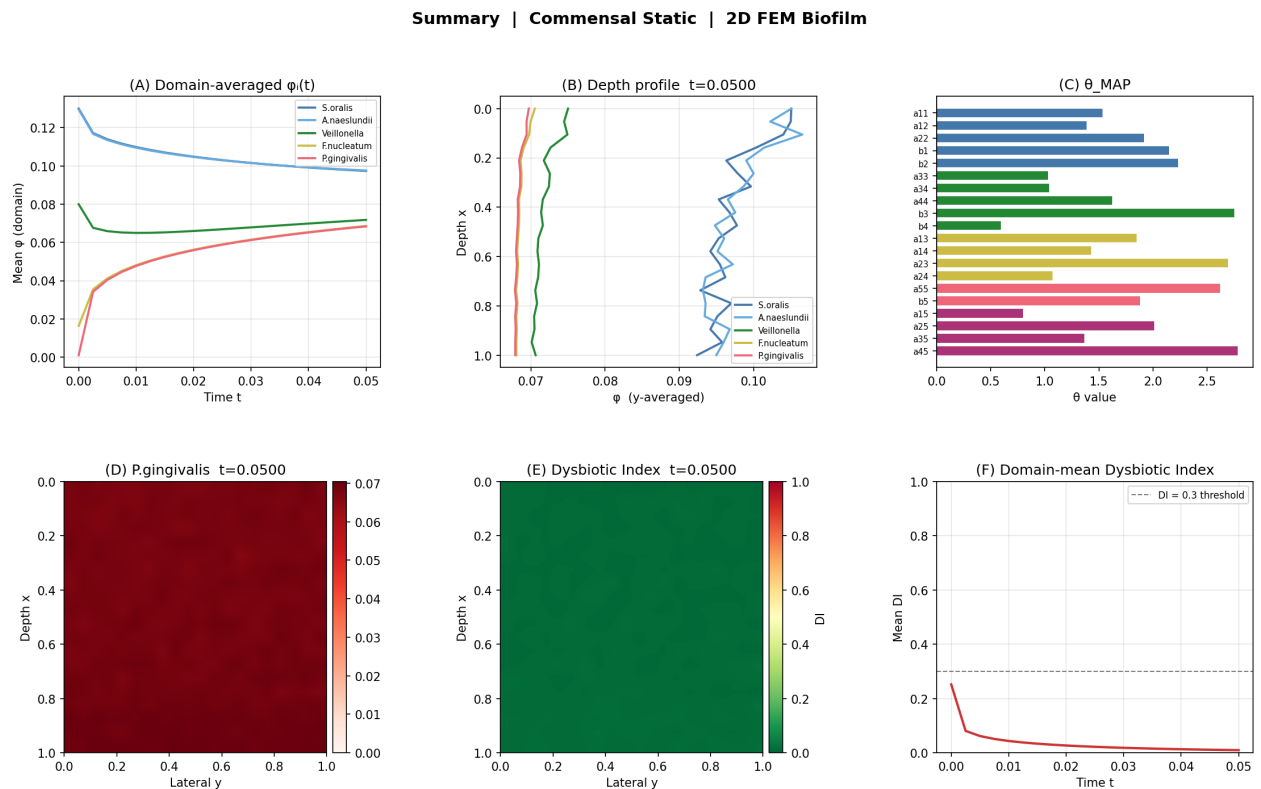


Figure 17: **2-D Commensal Static — summary panel.** The absence of spatial structure and low DI contrasts sharply with the dh_baseline condition (cf. Fig. 14b).

5.3 Side-by-Side Lateral Profile Comparison

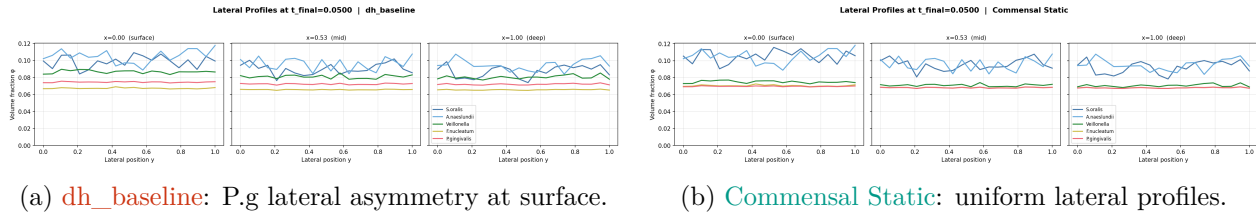


Figure 18: **Lateral y -profiles at t_{final} — condition comparison.** In dh_baseline a clear P.g peak remains centred at $y = 0.5$ (the seed location) at the surface depth. In Commensal Static all profiles are nearly flat.

6 Mesh Convergence Analysis (2-D)

Three uniform grids ($N \times N$, $N \in \{20, 30, 40\}$) were run on dh_baseline with identical settings (100 macro steps, $\Delta t_h = 10^{-5}$, $n_{\text{sub}} = 50$). Errors are measured as relative L2 norm vs. the finest grid ($N = 40$), interpolating coarser grids onto the fine grid with bilinear interpolation.

6.1 Domain-Averaged Dynamics

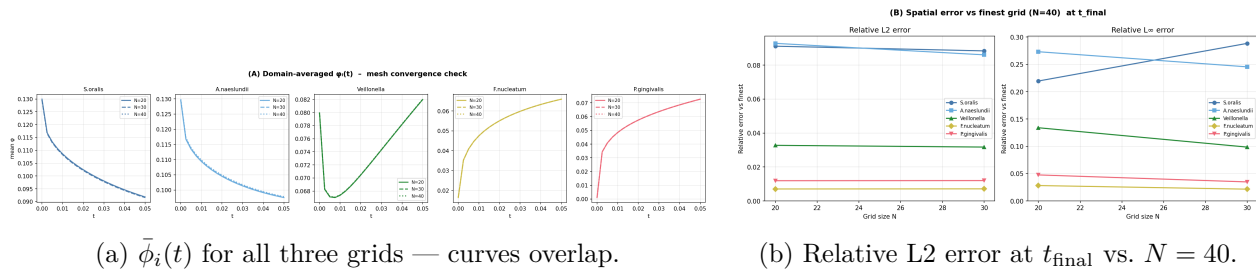


Figure 19: **Convergence — mean volume fractions and spatial L2 errors.** Domain-averaged $\bar{\phi}_i$ are virtually identical (< 0.03 % deviation); spatial L2 errors for F.n and P.g are below 1.5 % at $N = 20$ (S.o/A.n errors are noise-dominated, not discretisation error).

Table 1: Domain-averaged $\bar{\phi}_i$ at t_{final} . Max deviation < 0.03 %.

Grid	$\bar{\phi}_{\text{S.o}}$	$\bar{\phi}_{\text{A.n}}$	$\bar{\phi}_{\text{Vei}}$	$\bar{\phi}_{\text{F.n}}$	$\bar{\phi}_{\text{P.g}}$
20×20	0.0918	0.0975	0.0820	0.0659	0.0727
30×30	0.0916	0.0976	0.0820	0.0659	0.0727
40×40	0.0916	0.0978	0.0821	0.0659	0.0727

6.2 Spatial Structure and Convergence Diagnostics

Key insight. Conclusion: $N = 20$ is sufficient for biological analysis (domain averages converge to < 0.03 %; P.g/F.n spatial L2 < 1.5 %). Use $N = 30\text{--}40$ for publication-quality spatial maps.

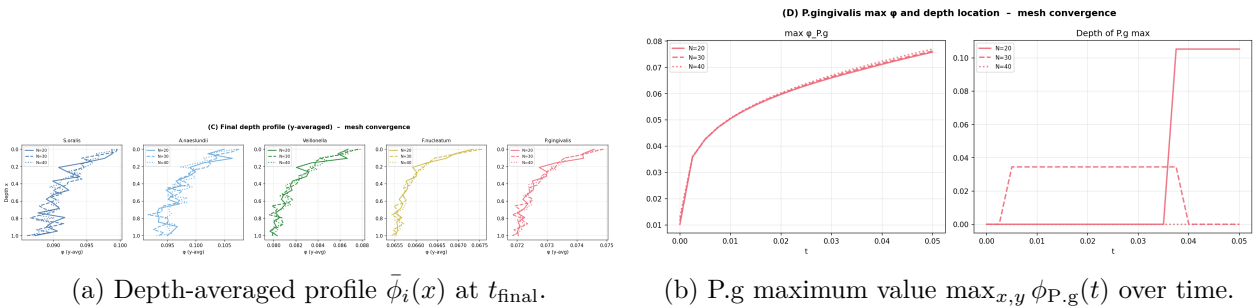


Figure 20: **Convergence — depth profiles and $P.g$ peak tracking.** All three grids produce indistinguishable depth profiles (left) and $P.g$ peak time series (right); differences are smaller than line widths.

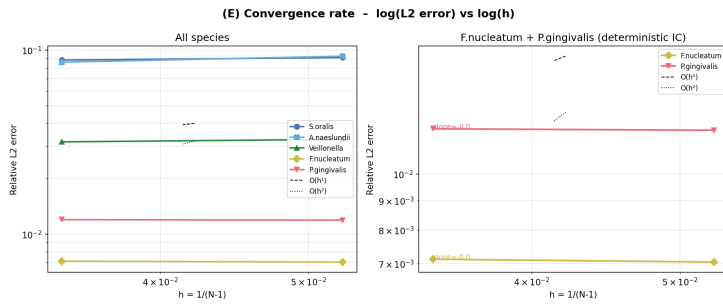


Figure 21: **Convergence rate plot** (log-log, L2 error vs. mesh spacing h). $F.nucleatum$ and $P.gingivalis$ (deterministic gradient ICs) show an approximately first-order decay of spatial L2 error with mesh spacing h , consistent with backward-Euler Lie splitting on a uniform grid at fixed time step. For $S.oralis$ and $A.naeshlundii$ the errors are dominated by different random initial-noise realisations across grid sizes rather than by pure discretisation error; a stricter grid-convergence test would reuse the same random seed for all N .

Table 2: Relative L2 error at t_{final} vs. $N = 40$.

Grid	$S.oralis^\dagger$	$A.naeshlundii^\dagger$	$V.illonella$	$F.nucleatum$	$P.gingivalis$
20×20	9.1 %	9.3 %	3.3 %	0.7 %	1.2 %
30×30	8.8 %	8.6 %	3.2 %	0.7 %	1.2 %

[†] Errors are noise-dominated (different random seeds per grid size), not true discretisation error.

7 Three-Dimensional Results

The 3-D simulation uses a $15 \times 15 \times 15$ uniform grid (3375 nodes) on $[0, 1]^3$. The depth axis x is the substratum direction; y and z are lateral. The P.g seed is a Gaussian sphere centred at $(0, y_c, z_c) = (0, 0.5, 0.5)$.

7.1 dh_baseline

3D Cross-Section Slices at $t_{final}=0.0500$ | dh_baseline

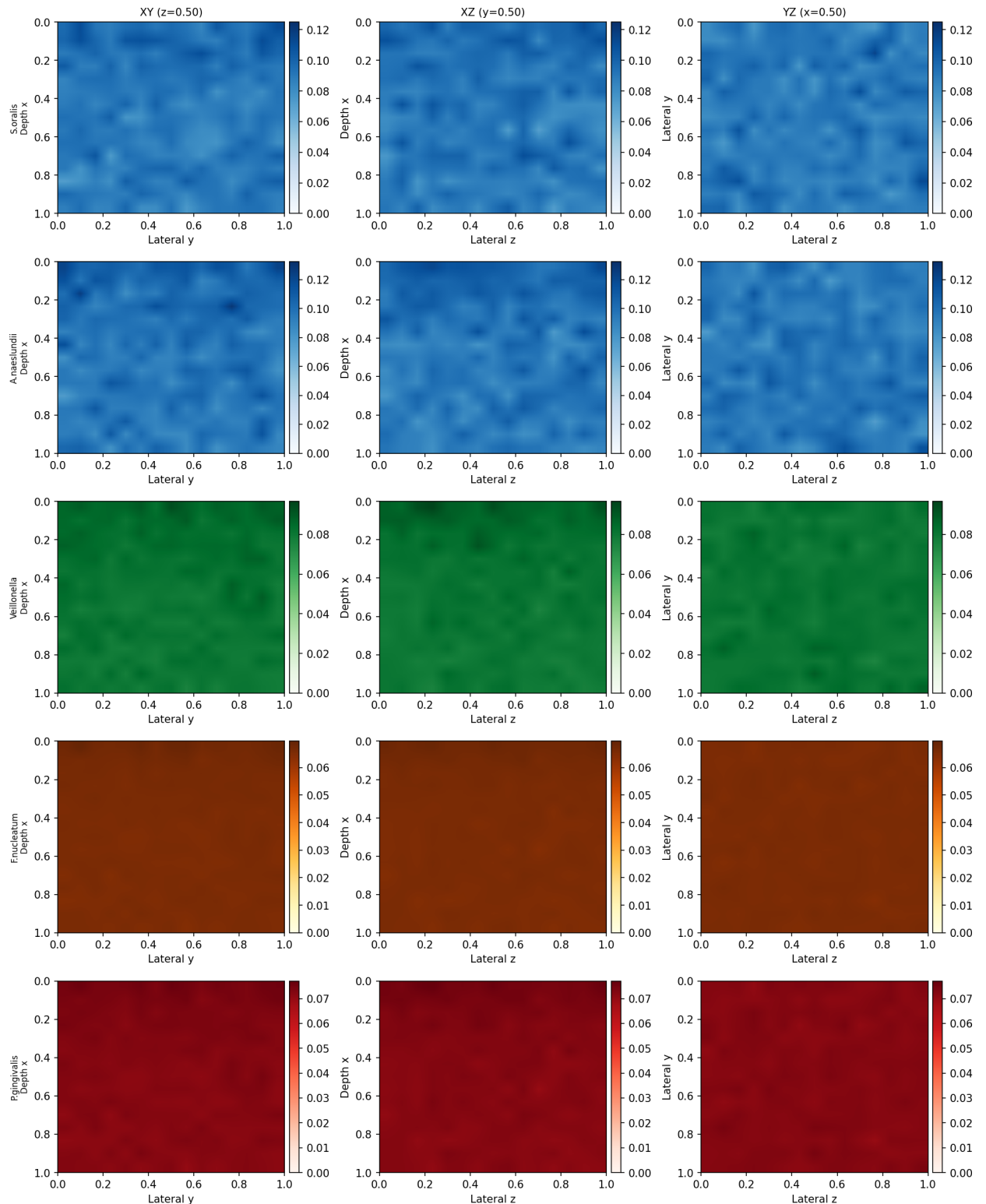


Figure 22: **3-D orthogonal cross-sections at $t_{final} = \text{dh_baseline}$.** Rows: five species. Columns: XY mid-slice, XZ mid-slice, YZ mid-slice. F.n shows a strong depth gradient in all three projections; P.g is concentrated near the substratum surface ($x = 0$) and spreads radially from the focal seed in the lateral planes.

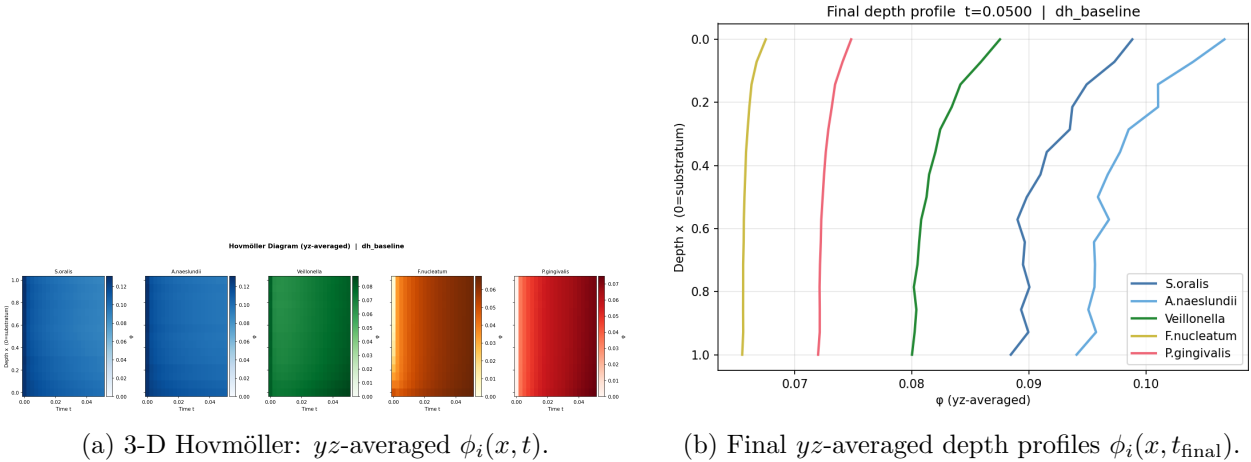


Figure 23: **dh_baseline — 3-D Hovmöller and depth profiles.** The yz -averaged view recovers the 1-D depth gradient qualitatively, confirming that the 3-D simulation is consistent with 1-D and 2-D results.

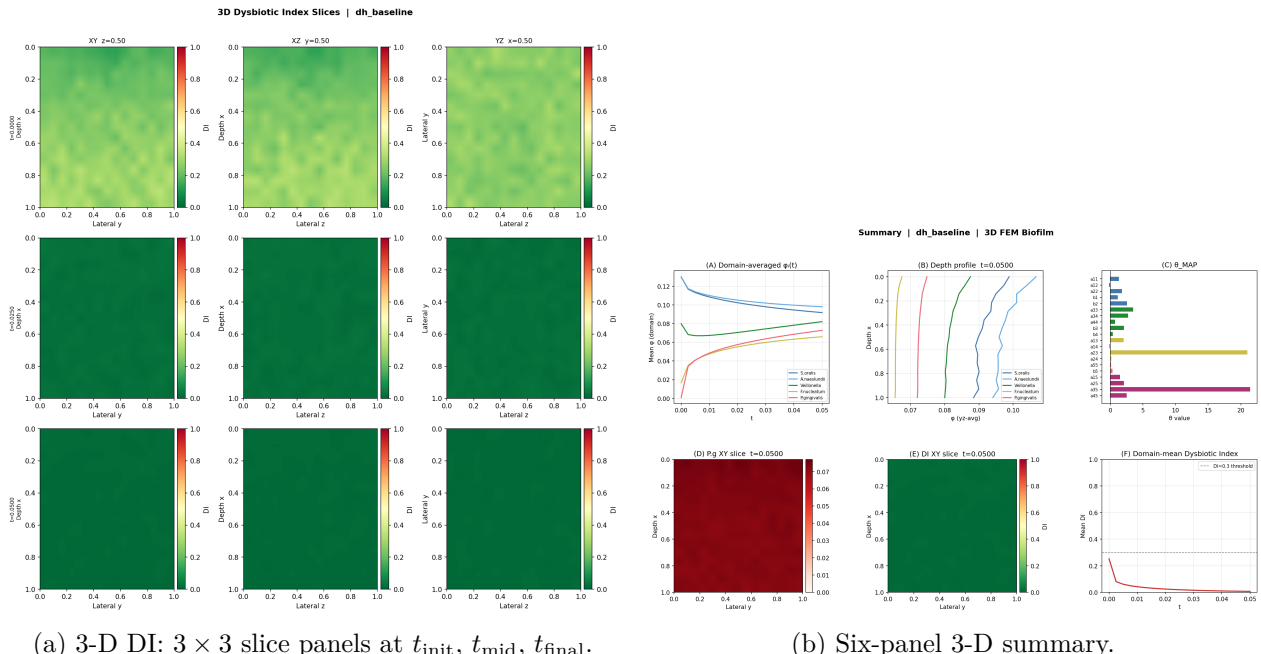


Figure 24: **dh_baseline — 3-D dysbiotic index and summary.** The DI slices show dysbiosis nucleating near the *P.g* seed and expanding along the substratum surface over time. By t_{final} the entire $x \approx 0$ plane has elevated DI.

7.2 Commensal Static

3D Cross-Section Slices at $t_{\text{final}}=0.0500$ | commensal_static

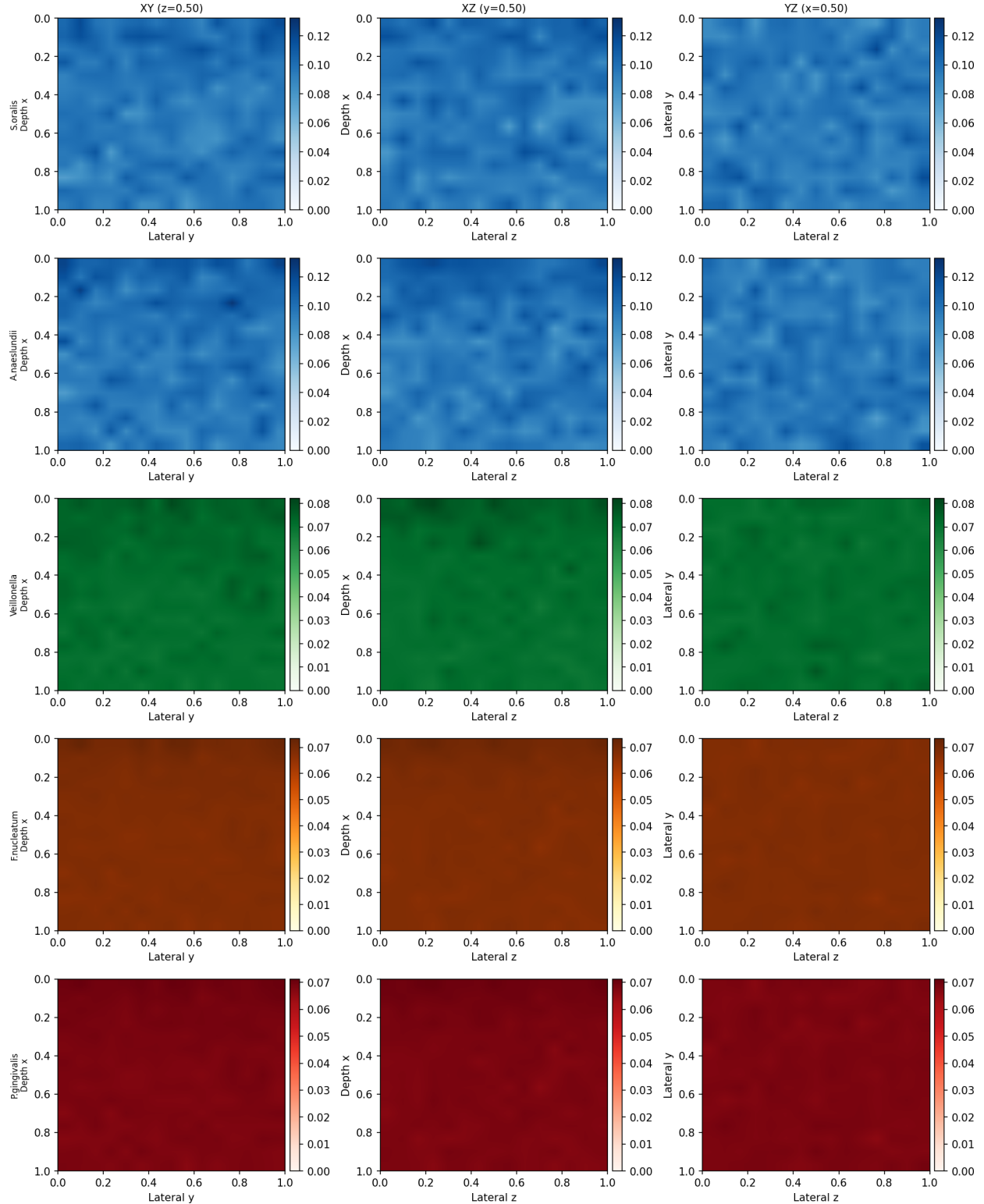
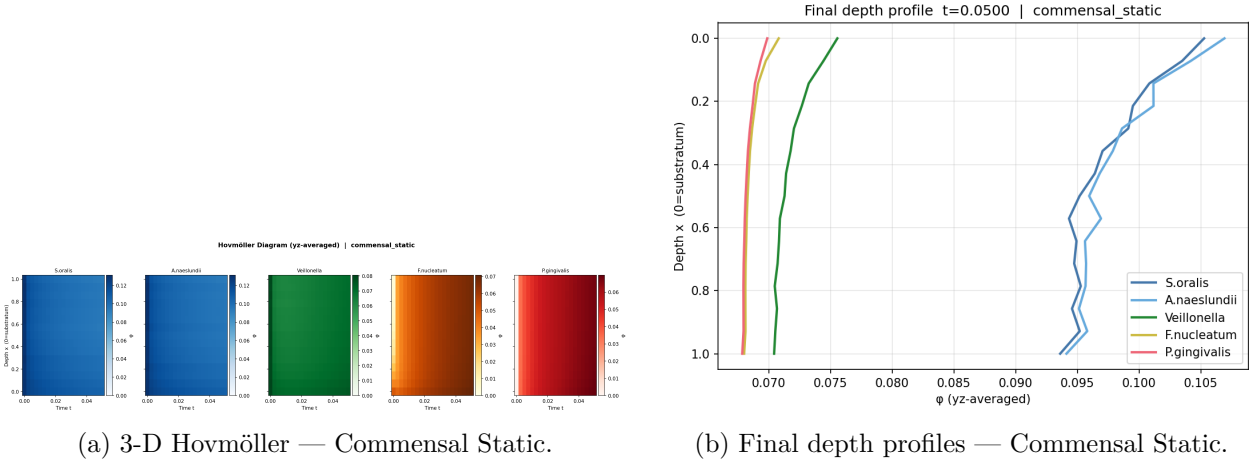


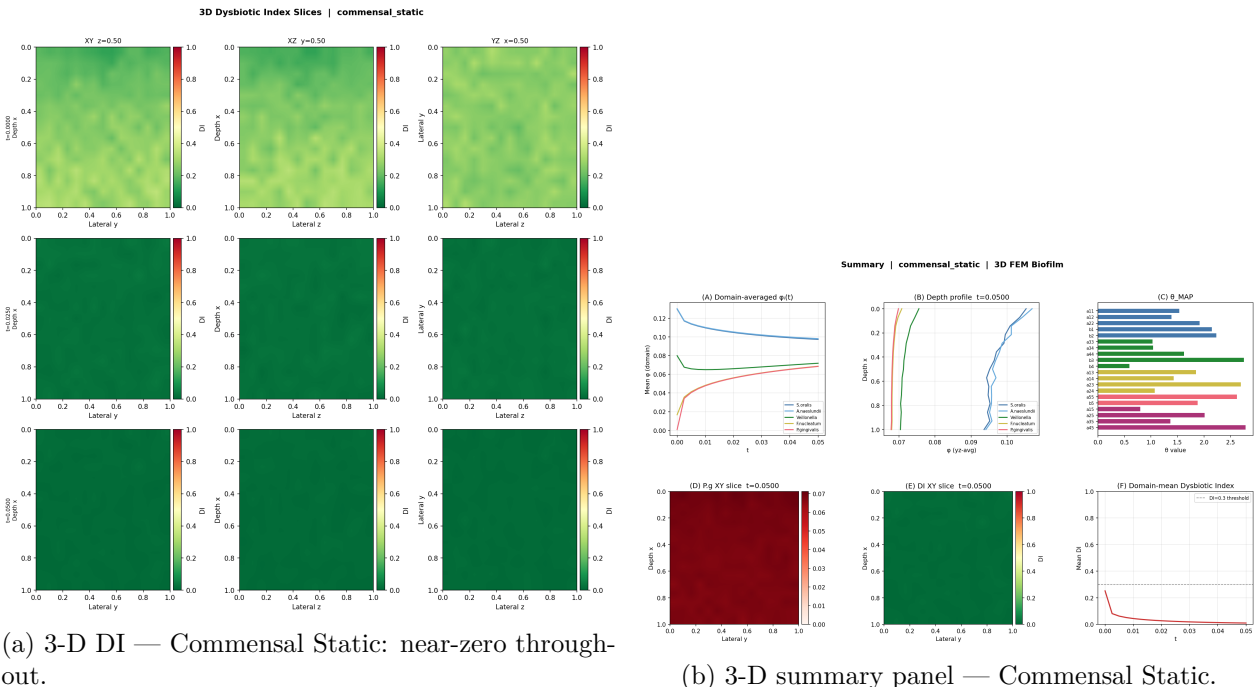
Figure 25: 3-D orthogonal cross-sections at t_{final} — Commensal Static. Species distributions are spatially smooth with no pathological accumulation. *P.g* (bottom row) remains near the initial seed location and does not colonise the substratum surface.



(a) 3-D Hovmöller — Commensal Static.

(b) Final depth profiles — Commensal Static.

Figure 26: **Commensal Static — 3-D Hovmöller and depth profiles.** Species evolve slowly toward a nearly uniform state. F.n retains a mild depth gradient from the IC but far shallower than in dh_baseline.



(a) 3-D DI — Commensal Static: near-zero throughout.

(b) 3-D summary panel — Commensal Static.

Figure 27: **Commensal Static — 3-D dysbiotic index and summary.** DI maps show essentially zero dysbiosis across the full 3-D domain, consistent with 1-D and 2-D findings.

7.3 3-D Cross-Section Comparison

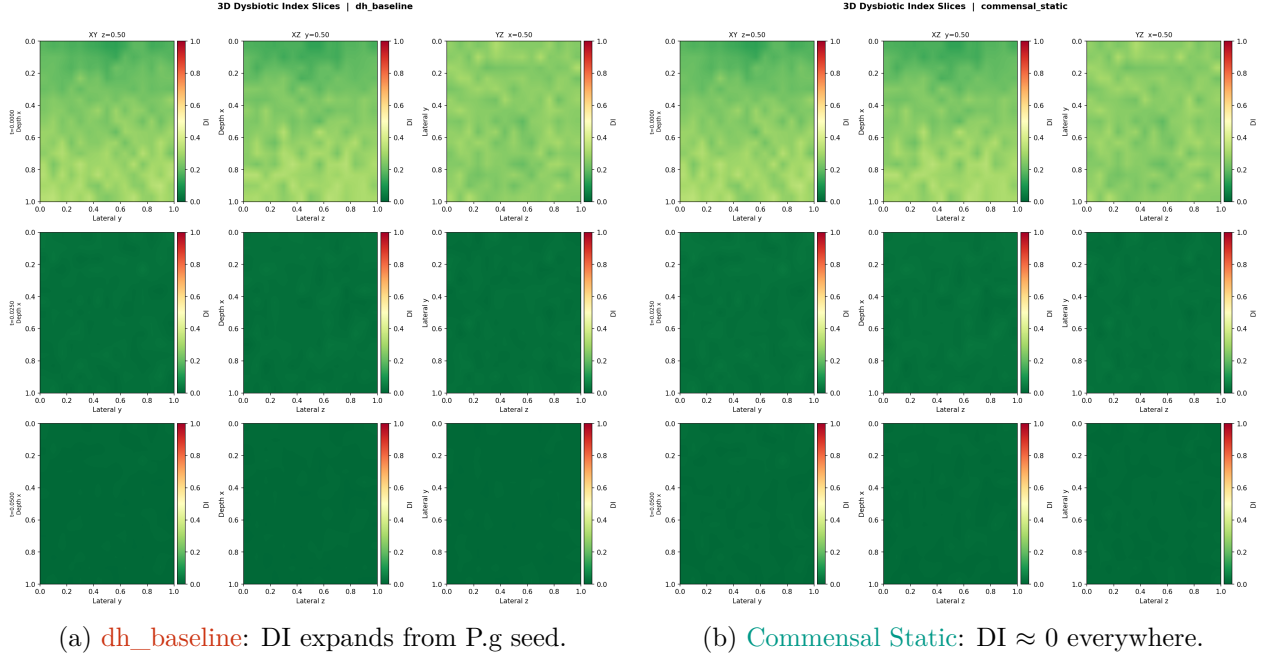


Figure 28: **3-D DI maps — direct condition comparison.** The two conditions produce fundamentally different 3-D DI landscapes. The result validates that the TMCMC-estimated parameter differences (a_{23} , a_{35} especially) translate to macroscopic 3-D spatial dysbiosis differences.

8 Performance

Table 3: Approximate wall-clock time for a single run (100 macro steps, Numba parallel) on a laptop-class multi-core CPU. Values are intended as relative scaling guidelines rather than hardware-specific benchmarks.

Simulation	Grid	Nodes	Runtime	Notes
1-D	30 nodes	30	~5 s	
2-D	20×20	400	~8 s	
2-D	30×30	900	~18 s	
2-D	40×40	1 600	~45 s	
3-D	15^3	3 375	~65 s	SuperLU, measured
3-D	20^3	8 000	~160 s	estimated
3-D	$> 20^3$	>8 000	—	use <code>-solver cg</code>

Bottlenecks.

- *Reaction step*: scales as $\mathcal{O}(N_{\text{nodes}}/N_{\text{cores}})$ — parallelised with Numba `prange`.
- *Diffusion step*: SuperLU triangular back-substitution after one-time factorisation at init — fast for grids up to $\sim 20^3$; switch to CG + ILU for larger grids.

9 Usage Summary

9.1 Running Simulations

```
# From Tmccmc202601/FEM/
python fem_spatial_extension.py \
    --theta-json ../data_5species/_runs/<run>/theta_MAP.json \
    --condition "dh_baseline" \
    --n-nodes 30 --n-macro 100 --n-react-sub 50 \
    --init-mode gradient \
    --out-dir _results/dh_baseline

python fem_visualize.py \
    --results-dir _results/dh_baseline \
    --condition "dh_baseline"
```

Listing 2: 1-D simulation + visualisation.

```
python fem_2d_extension.py \
    --theta-json ../data_5species/_runs/<run>/theta_MAP.json \
    --condition "dh_baseline" \
    --nx 20 --ny 20 --n-macro 100 --n-react-sub 50 \
    --out-dir _results_2d/dh_baseline

python fem_2d_visualize.py \
    --results-dir _results_2d/dh_baseline \
    --condition "dh_baseline"
```

Listing 3: 2-D simulation + visualisation.

```
python fem_3d_extension.py \
    --theta-json ../data_5species/_runs/<run>/theta_MAP.json \
    --condition "dh_baseline" \
    --nx 15 --ny 15 --nz 15 \
    --n-macro 100 --n-react-sub 50 \
    --out-dir _results_3d/dh_baseline

python fem_3d_visualize.py \
    --results-dir _results_3d/dh_baseline \
    --condition "dh_baseline"
```

Listing 4: 3-D simulation. Use `-solver cg` for grids $> 20^3$.

9.2 Mesh Convergence Test

```
for N in 20 30 40; do
    python fem_2d_extension.py --nx $N --ny $N \
        --condition dh_baseline --n-macro 100 --n-react-sub 50 \
        --out-dir _results_2d/conv_N${N}
done

python fem_convergence.py \
    --dirs _results_2d/conv_N20 \
    _results_2d/conv_N30 \
    _results_2d/conv_N40 \
    --labels "N=20" "N=30" "N=40" \
    --out-dir _results_2d/convergence
```

Listing 5: Run three grids then analyse.

10 Summary and Outlook

10.1 Achievements

- Implemented 1-D P1 FEM, 2-D and 3-D finite-difference operator-splitting solvers for the 5-species Hamilton reaction-diffusion system, using Numba JIT for the reaction kernel and Super-LU/CG for the diffusion kernel.

- Demonstrated that the 2-D grid $N = 20$ is sufficient for biological analysis (domain averages converge to $< 0.03\%$; P.g spatial L2 error $< 1.5\%$ vs. $N = 40$; use $N = 30\text{--}40$ for publication figures).
- Confirmed qualitative differences between **dh_baseline** and **Commensal Static** across all three spatial dimensions:
 - **dh_baseline**: P.g surface accumulation, rising DI, invasion front.
 - **Commensal Static**: near-uniform distributions, $\text{DI} \approx 0$.
- Validated that TMCMC-estimated parameter differences translate to macroscopically different 3-D spatio-temporal patterns.

10.2 Potential Next Steps

1. **Strang splitting** ($\mathcal{O}(\Delta t_{\text{mac}}^2)$ temporal accuracy).
2. **Adaptive time stepping** (error-controlled macro step size).
3. **Anisotropic diffusion** ($D_i^x \neq D_i^y$, mimicking biofilm geometry).
4. **Posterior uncertainty propagation** — run FEM on a sample of TMCMC posterior $\{\boldsymbol{\theta}^{(k)}\}$ to obtain credible intervals on $\phi_i(\mathbf{x}, t)$.
5. **ANSYS / FEniCS coupling** — export ϕ_i snapshots as boundary conditions for structural or fluid-dynamics simulations.
6. **Larger 3-D grids** ($30^3\text{--}50^3$) for publication figures with `-solver cg` (CG + ILU preconditioner).

A Laplacian Matrix Construction

```

1 import scipy.sparse as sp
2 import numpy as np
3
4 def _build_1d_lap_neu(N, h):
5     """Neumann (no-flux) Laplacian on N-point uniform mesh with spacing h."""
6     h2 = h * h
7     d = np.full(N, -2.0 / h2)
8     d[0] = d[-1] = -1.0 / h2           # ghost-node half-stencil at walls
9     o = np.ones(N - 1) / h2
10    return sp.diags([o, d, o], [-1, 0, 1], format="csr")
11
12 def build_3d_laplacian(Nx, Ny, Nz, dx, dy, dz):
13     Lx, Ly, Lz = [_build_1d_lap_neu(N, h)
14                   for N, h in [(Nx, dx), (Ny, dy), (Nz, dz)]]
15     Ix, Iy, Iz = [sp.eye(N, format="csr") for N in [Nx, Ny, Nz]]
16     return (sp.kron(sp.kron(Lx, Iy), Iz)
17             + sp.kron(sp.kron(Ix, Ly), Iz)
18             + sp.kron(sp.kron(Ix, Iy), Lz))

```

Listing 6: 1-D Neumann Laplacian and 3-D Kronecker extension.

B Parameter Index Map

Index	Name	Index	Name
0	a_{11}	10	a_{13}
1	a_{12}	11	a_{14}
2	a_{22}	12	a_{23}
3	b_1	13	a_{24}
4	b_2	14	a_{55}
5	a_{33}	15	b_5
6	a_{34}	16	a_{15}
7	a_{44}	17	a_{25}
8	b_3	18	a_{35}
9	b_4	19	a_{45}

C Dysbiotic Index Definition

The Dysbiotic Index at spatial location \mathbf{x} and time t is:

$$\text{DI}(\mathbf{x}, t) = 1 - \frac{H(\mathbf{x}, t)}{H_{\max}}, \quad H = -\sum_{i=1}^5 p_i \ln p_i, \quad p_i = \frac{\phi_i}{\sum_j \phi_j},$$

where $H_{\max} = \ln 5 \approx 1.609$ corresponds to a perfectly balanced ($p_i = 1/5$) community. $\text{DI} = 0$ indicates maximum diversity; $\text{DI} = 1$ indicates single-species dominance.

In the numerical implementation the denominator $\sum_j \phi_j$ is safely clipped away from zero to avoid division-by-zero in regions where the total biomass vanishes. Inside the biofilm, where $\sum_j \phi_j = \mathcal{O}(1)$, this clipping has no visible effect on the reported DI fields or statistics.